Redox-based sensing controls bacterial chemotaxis to copper

Gwennaëlle Louis[1], Pauline Cherry[1], Catherine Michaux[2], Sophie Rahuel-Clermont[3], Marc Dieu[4], Françoise Tilquin[1], Laurens Maertens[1,5], Rob Van Houdt[5], Patricia Renard[4], Eric Perpete[2] and Jean-Yves Matroule[1*]

[1]Research Unit in Biology of Microorganisms (URBM), Department of Biology, Namur Research Institute for Life Sciences (NARILIS), University of Namur, Namur, Belgium.

[2] Laboratoire de Chimie Physique des Biomolécules, Namur Research Institute for Life Sciences (NARILIS) and Namur Institute of Structured Matter (NISM), University of Namur, Rue de Bruxelles, 61, 5000 Namur, Belgium.

[3] Université de Lorraine, CNRS, IMoPA, F-54000 Nancy, France.

[4]MaSUN, Mass Spectrometry Facility, University of Namur, Namur, Belgium.

[5]Microbiology Unit, Interdisciplinary Biosciences, Belgian Nuclear Research Centre (SCK CEN), 2400 Mol, Belgium.

*Corresponding author. Mailing address: Research Unit in Biology of Microorganisms (URBM), 61 Rue de Bruxelles 5000 Namur, Belgium. Phone: (32)81-72-42-45. E-mail: jean-yves.matroule@unamur.be

Abstract

Chemotaxis is a widespread strategy used by unicellular and multicellular living organisms to maintain their fitness in stressful environments. In bacteria, the control of chemotaxis relies on the sensing of environmental changes by chemoreceptors, which modulate flagellar rotation via the well-characterized CheA-CheY two-component system. However, the molecular mechanisms underlying signal recognition and activation of the chemoreceptors remain largely unclear.

Here we address this gap in the frame of a chemotactic response sustaining bacterial flight from toxic copper (Cu). We found that a significant Cu accumulation in the cytosol triggers an oxidative stress, which can be abrogated by the overexpression of the superoxide dismutase SodB or of the catalase KatG. Interestingly, the inhibition of ROS production not only improves cell growth but also impedes Cu-chemotaxis, suggesting that ROS derived from cytosolic Cu mediate the control of Cu chemotaxis. We also provide evidence that cellular Cu accumulation favors Cu binding to the sensor domain of the newly identified chemoreceptor McpR. Finally, we discovered that the redox cycling of the McpR-bound Cu modulates McpR conformation. Overall our study provides mechanistic insights on a redox-based sensing by a chemoreceptor, indicating that the cellular redox status can play a key role in bacterial chemotaxis.

39 # Introduction

40 Cell motility is widely distributed across the three domains of life. For instance, in animals
41 it is involved in fertilization and in neutrophils recruitment to an inflammatory area. It also
42 allows archaea and bacteria to seek nutrients in scarce environments and to flee from toxic
43 compounds while it supports to some extent host tropism in the frame of symbiotic
44 relationships.

45 Most of the time, cell motility is driven by chemical gradients and is therefore named
46 chemotaxis. In flagellated bacteria, positive (attraction) and negative (repulsion) chemotactic
47 responses rely on the well characterized CheA-CheY two-component system that modulates
48 flagellar rotation, thereby inducing stochastic direction changes [1]. The activation state of
49 CheA-CheY is controlled by finely tuned cytoplasmic or inner membrane-spanning methyl-
50 accepting chemotaxis proteins (Mcp) monitoring chemical variations in the cytosol or in the
51 periplasm [2]. However, how the ligand is recognized and bound to the MCP and how this event
52 controls MCP activity is still largely unexplored.

53 Here we addressed this gap in chemotaxis regulation by deciphering a sensing mechanism
54 underlying the bacterial chemotactic response to a toxic Cu-rich environment. We provide
55 evidence that a high intracellular Cu concentration triggers the production of reactive oxygen
56 species (ROS), which is a prerequisite to Cu chemotaxis. We also demonstrate that the redox
57 cycling of a Cu ion bound to the sensor domain of the newly-identified McpR modulates McpR
58 conformation. This original redox sensing mechanism may ensure a continuous monitoring of
59 the intracellular Cu status, providing a real-time control of the chemotactic response.

60

61 # Results

62 In a previous study, we identified an original bimodal strategy to cope with Cu stress where
63 the flagellated morphotype (swarmer cells) of *C. crescentus* triggers a prompt negative
64 chemotaxis from the Cu source [3]. In the same study, we also showed that a significant
65 intracellular Cu accumulation is a prerequisite to sustain this chemotactic response, suggesting
66 that the sensing of Cu variations when the swarmer (SW) cell swims along the Cu gradient is
67 performed intracellularly.

68 In order to add a subcellular resolution to this Cu accumulation, we measured the Cu
69 content by ICP-OES in SW cell fractionates. In accordance with our previous study [3], Cu
70 exposure led to an important cellular Cu accumulation albeit at a much lesser extent in the
71 cytoplasm than in the periplasm (**Fig. 1A**).

72 The transient maintenance of a high intracellular Cu content in the SW cells may potentially
73 lead to an oxidative stress via the production of superoxide anion ($O_2^{\bullet-}$), hydrogen peroxide
74 (H_2O_2) and hydroxyl radical ($OH^{\bullet}$) (**Fig. S1A**). In line with this idea, the relative fluorescence
75 intensity of the ROS sensitive turn-on CellROX Deep Red probe is significantly increased in
76 SW cells exposed to Cu or H_2O_2, the latter being used as a positive control (**Fig. 1B**).
77 Accordingly, the fluorescence of the cytoplasmic turn-off rxYFP redox biosensor is partially
78 quenched under the same conditions (**Fig. 1C**), mirroring an imbalance of the cytoplasmic
79 GSH-GSSG pool upon oxidative stress (**Fig. S1B**). These findings are reinforced by the
80 differential expression of genes involved in oxidative stress response upon Cu stress, including
81 those encoding the catalase KatG (CCNA_03138) and the superoxide dismutases SodA
82 (CCNA_03672) and SodB (CCNA_01855) [4]. Together these data argue for the rapid
83 generation of an oxidative stress in SW cells exposed to Cu.

84 In order to determine whether the ROS derived from cellular Cu accumulation play a role
85 in Cu chemotaxis, we envisioned that boosting the aforementioned antioxidant defense system
86 would limit Cu-induced ROS production in SW cells. We ectopically expressed the *sodB* or the
87 *katG* genes in the WT background from the low copy pMR10 plasmid under the control of the
88 strong and constitutive lac promoter. The resulting $sodB^+$ and $katG^+$ strains prevent the increase
89 of the CellROX Deep Red fluorescence upon Cu exposure, reflecting a potentiation of
90 antioxidant defenses (**Fig. 1D**). In support of this data, the growth of these two optimized $sodB^+$
91 and $katG^+$ strains is significantly improved under moderate Cu stress (**Fig. 1E**), arguing for a
92 role of $O_2^{\bullet-}$, H_2O_2 in Cu toxicity.

93 In order to assess the potential role of these ROS in Cu chemotaxis, we took advantage of
94 the aforementioned $sodB^+$ and $katG^+$ strains, where ROS formation is largely hindered. By
95 using the previously designed Live Chemotaxis Imaging (LCI) [3], we showed that the $sodB^+$
96 and $katG^+$ strains are impaired in Cu chemotaxis, at a similar extent to the Δ*cheA1* mutant (**Fig.**
97 **1F**, **SI Appendix**). Consistent with a role of KatG in H_2O_2 detoxification, the $katG^+$ strain is
98 also impeded in H_2O_2 chemotaxis (**Fig. S2**). These data support a major role of the ROS
99 resulting from Cu accumulation in Cu chemotaxis.

100 To further dissect the detailed mechanisms of Cu sensing, we sought to identify the
101 chemoreceptor involved in Cu chemotaxis. The genome of *C. crescentus* is predicted to encode
102 19 Mcp (named McpA to McpS) [5]. No canonical Cu binding site, including the CXXC motif
103 or the βαββαβ fold [6], could be found by running manual and JPred4-based analyses of the
104 19 Mcp sequences [7]. Therefore, we proceeded to single in-frame deletions of the 19 *mcp*
105 genes, and their respective chemotactic behavior to Cu was assessed by LCI (**Fig. 2A**). Most of
106 the Δ*mcp* mutants displayed a WT-like behavior with a flight percentage after 25 min varying
107 between 15% and 51%. Only Δ*mcpA*, Δ*mcpB* and Δ*mcpR* mutants did not significantly cross

108 the arbitrary threshold of 10% flight, suggesting that Cu chemotaxis might be severely affected
109 in these genetic backgrounds. The Δ*mcpA*, Δ*mcpB* and Δ*mcpR* mutants could be complemented
110 by the expression of an ectopic version of *mcpA*, *mcpB* and *mcpR* on the low copy pMR10
111 plasmid, respectively, suggesting that they may potentially control Cu chemotaxis (**Fig. S3**).
112 However, McpA and McpB are likely involved in chemotaxis at a more global extent
113 considering (i) the position of the *mcpA* and *mcpB* genes within and in the vicinity of the major
114 chemotaxis cluster, respectively [8], and (ii) the reduced motility halo of the Δ*mcpA* mutant
115 observed in a Cu-free swarming assay (**Fig. S4**). In addition, McpB displays the terminal
116 sequence of the CheB/CheR docking site that may be necessary for the adaptive response [9],
117 which will not be considered in this study. Therefore, we aimed at further characterizing the
118 role of McpR in Cu chemotaxis.

119 Owing to the multimeric organization of Mcp clusters in bacteria [10], one may argue that
120 the loss of Cu chemotaxis in the Δ*mcpR* mutant results from a loss of motility and/or a disruption
121 of the general chemotactic machinery. The ability of the Δ*mcpR* mutant to form a motility halo
122 in a Cu-free swarming assay (**Fig. S5A**) and to sustain negative chemotaxis to other chemicals,
123 such as zinc (Zn) (**Fig. S5B**), refutes this hypothesis. It is also worth mentioning that the loss
124 of Cu chemotaxis in the Δ*mcpR* mutant is not due to a loss of ROS production under Cu stress
125 since the Δ*mcpR* mutant exhibits a similar decrease of the rxYFP fluorescence to the WT strain
126 upon Cu exposure (**Fig. S6**).

127 Mcp are able to sense attractants or repellents in a direct or indirect manner [11]. Therefore,
128 we decided to assess by intrinsic fluorescence spectroscopy the direct binding of Cu to purified
129 McpR. When mixed with Cu(I) or Cu(II) at 1:1, 1:10 and 1:100 ratios, the intrinsic McpR
130 fluorescence at 346 nm is quenched in a dose-dependent manner, reflecting a modification of
131 the McpR aromatic residues environment (**Fig. 2B**, see **Fig. S7** for full spectra). The

132 dissociation constants (*K*d) of 48 µM +/- 10 µM and 37 µM +/- 9 µM for Cu(I) and Cu(II),
133 respectively, attest to a similar affinity of both ionic forms for McpR. However, the micromolar
134 range of Cu(I) and Cu(II) *K*ds exceeds from several logs the *K*d of well-known cuproproteins
135 [12, 13], arguing for a rather low affinity of McpR for Cu. Therefore, one may argue that the
136 high Cu cellular content measured in the Cu-exposed SW cells is necessary to promote a rather
137 labile interaction between McpR and Cu. Interestingly, McpR seems to preferentially bind Cu
138 since Zn, cadmium (Cd), manganese (Mn) and nickel (Ni) had no effect on McpR intrinsic
139 fluorescence (**Fig. S8**).

140 The complete loss of Cu-chemotaxis in the *sodB*+ and *katG*+ genetic backgrounds (**Fig.**
141 **1F**) indicates that Cu binding to McpR is solely not sufficient to sustain Cu chemotaxis.
142 Consistent with this idea, we found that H_2O_2 chemotaxis is fully abolished in the Δ*mcpR*
143 mutant, indicative of a role of McpR as a sensor of the oxidative stress (**Fig. 2C**). Owing to the
144 oxidative conditions generated by Cu accumulation in the cytosol (**Fig. 1B-C**), we sought to
145 assess by LC/MS the oxidation status of McpR with a particular focus on the sensor domain
146 (residues 1-161) after incubating purified McpR with Cu(II) or Cu(I) +/- H_2O_2 at a 1:100 ratio.
147 Only the Cu(I) + H_2O_2 condition, and to a lesser extent Cu(I), led to a significant oxidation of
148 the McpR sensor domain, and more specifically of the H99 residue. In this particular condition,
149 about 30% of the H99 residues acquired an additional oxygen ion, most likely yielding 2-
150 oxoHis (**Fig. 3A**). In accordance with this observation, the expression of an ectopic $mcpR_{H99A}$
151 allele in the Δ*mcpR* mutant does not restore its ability to sustain Cu chemotaxis, indicating that
152 H99 is a key residue in McpR Cu chemotaxis (**Fig. 3B**). Noteworthy, H99A mutation does not
153 impede Cd chemotaxis for which McpR is also essential (**Fig. S9**), confirming the functionality
154 of $McpR_{H99A}$ and the proper assembly of the chemotactic machinery.

155 Metal catalyzed oxidation (MCO) of histidines via the generation of $OH^{\bullet}$ has been
156 previously described in the *Bacillus subtilis* PerR repressor [14], in yeast SOD1 [15], and in
157 amyloid beta (Aβ) peptide [16]. The exact role of this modification remains unknown. In
158 addition, no redox cycling involving 2-oxoHis has been described so far, questioning the
159 relevance of H99 oxidation in Cu/ROS sensing. MCO mostly targets the metal-binding residues
160 in a caged process [17], suggesting that H99 may coordinate Cu. To test this hypothesis, we
161 calculated the *K*d values of the $McpR_{H99A}$/Cu(I) and $McpR_{H99A}$/Cu(II) complexes (**Fig. 3C**).
162 H99A mutation triggers a 9.4- and 5.8-fold increase of Cu(I) and Cu(II) *K*d, respectively,
163 relative to McpR, suggesting a key role of H99 in Cu(I) and Cu(II) coordination. The important
164 variability associated with the $McpR_{H99A}$ *K*d values likely reflects a potential instability of this
165 mutant in solution upon Cu(I) and Cu(II) exposure, resulting in the presence of several
166 subpopulations of $McpR_{H99A}$.

167 McpR sequence analysis by the TMHMM 2.0 [18] and SignalIP 6.0 [19] tools did not
168 reveal any McpR transmembrane domains and signal peptide, respectively, arguing for a
169 cytoplasmic McpR localization and therefore a Cu sensing. The 3D structure prediction of
170 McpR by a fold recognition method (Phyre2 [20]) highlights a cysteine (C75) residue in the
171 vicinity of H99 (**Fig. 3D**). Cysteine residues often contribute to Cu coordination and the
172 measured 19.8 Å distance in the predicted model is compatible with Cu coordination by C75
173 and H99 residues [21]. In line with this idea, a Δ*mcpR* mutant expressing an ectopic $mcpR_{C75S}$
174 allele was unable to trigger Cu chemotaxis (**Fig. 3B**), indicating that C75 also plays a key role
175 in Cu-sensing. As a control, the $McpR_{C75S}$ mutant was still able to flee from H_2O_2, for which
176 McpR is also required (**Fig. S10**), attesting the functionality of the $McpR_{C75S}$ mutant within the
177 chemotaxis machinery. In order to determine whether the loss-of-function of the $McpR_{C75S}$
178 mutant in Cu chemotaxis resulted from a loss of Cu binding, we calculated the *K*d values of the
179 $McpR_{C75S}$/Cu(I) and $McpR_{C75S}$/Cu(II) complexes. Similar to the H99A mutation, the C75S

180 mutation also impeded Cu(I) binding as attested by a 3.5-fold *K*d increase. Surprisingly, Cu(II)
181 binding to the $McpR_{C75S}$ mutant remained unchanged (**Fig. 3C**), suggesting that C75 is required
182 to coordinate Cu(I) but not Cu(II). Consistent with this observation, H99 oxidation by Cu(I) +/-
183 H_2O_2 is fully abolished in the $McpR_{C75S}$ mutant (**Fig. 3E**). The *K*d values calculated for the
184 $McpR_{C75S}$ and $McpR_{H99A}$ mutants are in agreement with the known selective binding of Cu(I)
185 and Cu(II) to cysteine and histidine residues, respectively [21, 22].

186 The aforementioned observations led us to the idea that Cu(I) coordination by H99 and
187 C75 is decisive for McpR-mediated Cu chemotaxis. Given the structural changes elicited by
188 the binding of a ligand to a cognate chemoreceptor [23], we envisioned that Cu(I) binding to
189 McpR modulates its conformation. To test this idea, Far-UV circular dichroism (CD)
190 spectroscopy was used to monitor the impact of Cu(I) and Cu(II) on McpR secondary structure.
191 Accordingly, Cu(I) has a more significant impact than Cu(II) on McpR secondary structure
192 (**Fig. 3F**), increasing the α-helix percentage from 23% to 44%.

193 Based on our findings, we propose that Cu excess within the cytoplasm catalyzes the
194 production of ROS including $O_2^{\bullet-}$ and H_2O_2 that are required for Cu chemotaxis. Cu excess also
195 favors a rather labile Cu binding to the McpR sensor domain. Cu(I) coordination by McpR C75
196 and H99 residues triggers McpR conformational change. Interestingly, Cu(II) only binds McpR
197 H99 residue and does not modify the apo form-like conformation. These observations suggest
198 that a redox cycling of the McpR-bound Cu atom could modulate McpR conformation (**Fig. 4**).

199 # Discussion

200 Although the signaling pathway controlling flagellar rotation in bacterial chemotaxis has
201 been extensively studied, the sensing mechanisms by the upstream chemoreceptors (MCP) are

202 still largely unknown. We sought to address this gap in the frame of negative chemotaxis to
203 toxic copper (Cu) in the bacterial model *Caulobacter crescentus*.

204 Our study identified the first Cu sensing MCP hereafter named McpR. McpR is devoid of
205 any transmembrane domains or signal peptide and is therefore predicted to localize in the
206 cytoplasm. Cytoplasmic MCPs have been shown to monitor the cellular metabolic state [24],
207 whereas inner membrane MCPs usually sense the periplasmic environment, as a proxy for
208 extracellular changes. The cytoplasmic Cu content is significantly increased albeit to a lesser
209 extent than in the periplasm when the SW cells are exposed to a toxic Cu concentration. To
210 explain the rationale of using a cytoplasmic MCP to monitor extracellular changes, one could
211 hypothesize that the sensing of cytoplasmic Cu provides a more sensitive monitoring of subtle
212 variations of Cu concentrations when the SW cell swims down a Cu gradient.

213 In a previous study, we showed that the maintenance of a high cellular Cu concentration is
214 critical for Cu chemotaxis [3]. Here, we provide evidence that McpR binds Cu with low affinity,
215 suggesting that this binding is only possible when the Cu concentration within the cytoplasm is
216 high. Considering that Cu binding to McpR is a prequisite for Cu chemotaxis, one could propose
217 that when the SW cell swim away from the Cu source, the cytoplasmic Cu concentration
218 decreases and ultimately impede Cu binding to McpR and the resulting chemotactic signaling
219 pathway.

220 We also demonstrate that the cellular Cu accumulation triggers by an unknown mechanism
221 the production of ROS that can be impeded by the overexpression of SodB and KatG catalase,
222 suggesting that at least $O_2^{\cdot -}$ and H_2O_2 are generated. The contribution of the ROS generated by
223 cellular Cu in Cu toxicity is still largely debated [25, 26]. Here, we demonstrate that ROS
224 derived from cellular Cu not only impede cell growth to some extent, but also play a key role
225 in Cu chemotaxis. The exact target of ROS in Cu chemotaxis was not identified in this study
226 but one could hypothesize that $O_2^{\cdot -}$ is rapidly converted into H_2O_2. The latter would feed a local

227 Fenton-like reaction catalyzed by the Cu-(I) atom coordinated by McpR C75 and McpR H99
228 residues. This would lead to a local OH· production and to the oxidation of McpR-bound Cu(I)
229 into McpR-bound Cu(II). Owing to the reducing cytoplasmic environment, McpR-bound Cu(II)
230 could in turn be reduced by cytoplasmic electron donors such as GSH, NADH and thioredoxin
231 to restore the Cu(I) ionic form. Thereby, the McpR-bound Cu would undergo a redox cycling
232 involving the Cu-(I) and Cu-(II) ionic forms, which would be maintained as long as H_2O_2 is
233 produced by cytoplasmic Cu. Cu-generated ROS would therefore act as second messengers in
234 a bacterial stress response.

235 The modulation of the CheA-CheY two-component system results from MCP
236 conformational changes occurring upon ligand binding [27]. We demonstrated here that McpR
237 conformation is modulated by the ionic status of the Cu atom bound to McpR. It should be
238 emphasized that MCPs are usually organized in trimers of dimers and assembled in large arrays
239 in cells [28]. Therefore, it is possible that Cu coordination by McpR C75 and McpR H99
240 residues within the McpR array implies two McpR monomers from one or two distinct dimers.
241 Nevertheless, McpR conformational change likely regulates the downstream effectors and the
242 resulting chemotactic response.
243

244 Materials and Methods
245

246 **Strains, plasmids and growth conditions**

247 *Caulobacter crescentus* (NA1000 strain) was grown at 30°C in Peptone Yeast Extract (PYE)
248 medium [29] with 5 µg/ml kanamycin, 1 µg/ml chloramphenicol and/or an appropriate
249 concentration of $CuSO_4.5H_2O$ when required. Cultures in exponential phase were used for all
250 experiments. Strains and plasmids are listed in Table S1, and the strategies for their construction
251 are available upon request. SW cells isolation was achieved according to [30].

252 **Growth curve measurements**

253 *C. crescentus* exponential phase cultures were diluted in PYE medium to a final $O.D._{660\ nm}$ of
254 0.05 and inoculated in 96-well plates with appropriate $CuSO_4$ concentration when required.
255 Bacteria were then grown for 24 h at 30°C under continuous shaking in an Epoch 2 Microplate
256 Spectrophotometer from BioTek (Santa Clara, CA, USA). The absorbance at $O.D._{660\ nm}$ was
257 measured every 10 min.

258 **Motility assay**

259 *C. crescentus* cultures grown in PYE were diluted to an $O.D._{660\ nm}$ of 0.4 and inoculated with
260 sterile toothpicks on a PYE swarming plates (PYE + 0.25% agar). The plates were incubated at
261 30°C for 3 days, then scanned.

262 **Cellular fractionation and ICP-OES measurements**

263 *C. crescentus* cells were fixed for 20 min in 2% paraformaldehyde at 4°C and then washed three
264 times with an ice-cold wash buffer (10 mM Tris-HCl pH 6.8, 100 µM EDTA). The cells were
265 then incubated with 0.125% zwitterionic detergent. A final centrifugation at 14,500 x g for 15
266 min separated the cytoplasm (and inner membrane fraction) from the periplasm (and outer
267 membrane fraction). The two fractions were incubated overnight with a final concentration of
268 1 M HNO_3 and then analyzed by inductively coupled plasma - optical emission spectrometry
269 (ICP-OES) with an Optima 8000 ICP-OES from PerkinElmer. Cellular Cu concentration were
270 calculated as described in [3].

271 **Oxidative stress measurement with the CellROX Deep Red probe**

272 An exponential phase culture of *C. crescentus* was synchronized to isolate the SW cells. The
273 isolated SW cells were diluted to an OD_{660nm} of 0.2 and incubated for 30 min at 30°C under
274 moderate shaking with 5 µM of CellROX Deep Red probe (ThermoFisher) and appropriate
275 concentrations of $CuSO_4$ or H_2O_2. The bacteria were then washed three times with 20 mM

276 Phosphate Buffer to remove the non-internalized probes. The bacteria were finally transferred
277 into a black bottom 96-wells plate and the fluorescence was monitored at 640/690 nm with a
278 SpectraMax iD3 (Molecular Devices, San Jose, CA, USA).

279 **Oxidative stress measurement with the rxYFP biosensor**

280 The SW cells were isolated from an exponential phase culture overexpressing the rxYFP
281 biosensor [31]. The SW cells were diluted to an OD_{660nm} of 0.4 in a black bottom 96-well plate
282 and mixed with different concentrations of $CuSO_4$ and H_2O_2. The rxYFP fluorescence was then
283 monitored every minute for 20 min at 510/556 nm with a SpectraMax iD3 (Molecular Devices,
284 San Jose, CA, USA).

285 **Live Chemotaxis Imaging**

286 The live chemotaxis imaging (LCI) assay was adapted from[3]. Eight microliters of melted
287 1.5% agarose H_2O with $CuSO_4$, H_2O_2, $ZnSO_4$ or $CdSO_4$ were loaded into the chamber through
288 the external inlet channels to generate the plug. One hundred and fifty microliters of isolated
289 SW cells were in turn injected into the bacterial chamber through the central inlet channel.
290 Images were collected every min for 25 min in one focal plan (near the liquid surface) in the
291 vicinity of the plug with a Nikon Eclipse Ti2-E inverted microscope equipped with a Nikon
292 20X/0.5 Ph2 objective and with a Hamamatsu C13440 digital camera. Quantitative analysis of
293 the time-lapse images was performed with MicrobeJ [32]. The number of bacteria in a same
294 focal plane was determined at each time point.

295 **Protein expression and purification**

296 A BL21 pET28a-$McpR_{His}$ exponential phase culture was incubated for 3 h under shacking at
297 37°C with 1 mM Isopropyl-β-D-thiogalactopyranoside (IPTG) and then harvested by
298 centrifugation for 30 min at 4,000 x g at 4°C. $McpR_{His}$ induction was verified by 12 % Tricine–
299 sodium dodecyl sulfate–polyacrylamide gel electrophoresis (Tricine–SDS–PAGE), followed

300 by Coomassie Blue staining and by WB using an anti-His antibody (1/5000). In order to purify
301 $McpR_{His}$, the IPTG-induced culture was washed with 0.1 M phosphate buffer (pH 8) and
302 centrifuged for 15 min at 9,000 x g at 4°C. Bacterial cells were lysed at 2.4 kbar using a Cell
303 disruptor (Cell Disruption System – one shot model, Constant). As $McpR_{His}$ was mainly
304 forming inclusion bodies, the pellet fraction was resuspended for 1 h under shaking at 4°C in a
305 0.1 M phosphate buffer (pH 8) containing 6 M guanidine. The solubilized inclusion bodies were
306 centrifuged for 30 min at 9,000 x g at 4 °C. The collected supernatant was dialyzed overnight
307 in a 0.1 M phosphate buffer (pH 8) to remove guanidine.

308 **Fluorescence quenching by Cu and other metal ions**

309 McpR protein concentration was determined (i) by measuring the absorbance of the sample at
310 280 nm with the SpectraMax iD3 or (ii) with a Bradford protein assay. 3.58 µM of McpR was
311 incubated with different ratios of $CuSO_4$, Tetrakis(acetonitrile)copper(I) hexafluorophosphate,
312 $ZnSO_4$, $CdSO_4$, $MnSO_4$ and $NiSO_4$ in black bottom 96-wells plates. The fluorescence emission
313 spectra were recorded upon 280 nm excitation with the SpectraMax iD3.

314 **Kd determination**

315 The titration of McpR by Cu(I) or Cu(II) monitored by the protein intrinsic fluorescence
316 intensity quenching was fitted to a single-site hyperbolic model by non-linear regression using
317 the Scidavis 2.7 software to determine the affinity constants. Dissociation constants are reported
318 as the mean value ± standard deviation obtained from a minimum of three independent
319 experiments performed on distinct protein productions.

320 **Identification of McpR oxidation by mass spectrometry**

321 *Protein digestion*

322 McpR samples were treated using Filter-aided sample preparation (FASP) using the following
323 protocol. To first wash the filter, 100 µl of formic acid 1 % were placed in each Millipore

324 Microcon 30 MRCFOR030 Ultracel PL-30 before a 15 min centrifugation at 14,100 x g. For
325 each sample, 40 µg of protein adjusted in 150 µl of 8 M urea buffer (8 M urea in 0.1 M Tris
326 buffer at pH 8.5) were placed individually in a column and centrifuged for 15 min at 14,100 x
327 g. The filtrate was discarded and the columns were washed three times by adding 200 µl of urea
328 buffer followed by a 15 min centrifugation at 14,100 x g. For the reduction step, 100 µl of
329 dithiothreitol (DTT) were added and mixed for 1 min at 400 rpm with a thermomixer before a
330 15 min incubation at 24 °C. The samples were then centrifugated for 15 min at 14,100 x g, the
331 filtrate was discarded and the filter was washed by adding 100 µl of urea buffer before another
332 15 min centrifugation at 14,100 x g. An alkylation step was performed by adding 100 µl of
333 iodoacetamide ((IAA), in urea buffer) in the column and mixing for 1 min at 400 rpm in the
334 dark followed by a 20 min incubation in the dark and a 10 min centrifugation at 14,100 x g. To
335 remove the excess of IAA, 100 µl of urea buffer were added and the samples were centrifuged
336 for 15 min at 14,100 x g. To quench the rest of IAA, 100 µl of DTT were placed on the column,
337 mixed for 1 min at 400 rpm and incubated for 15 min at 24 °C before a 10 min centrifugation
338 at 14,100 x g. To remove the excess of DTT, 100 µl of urea buffer were placed on the column
339 and centrifuged for 15 min at 14,100 x g. The filtrate was discarded and the column was washed
340 three times by adding 100 µl of 50 mM sodium bicarbonate buffer ((ABC), in ultrapure water)
341 followed by a 10 min centrifugation at 14,100 x g. The remaining 100 µl were kept at the bottom
342 of the column to avoid any evaporation in the column. The digestion process was performed by
343 adding 80 µl of mass spectrometry grade trypsin (1/50 in ABC buffer) in the column and mixed
344 for 1 min at 400 rpm followed by an overnight incubation at 24°C in a water saturated
345 environment. The Microcon columns were placed in a 1.5 ml LoBind tube and centrifuged for
346 10 min at 14,100 x g. Fourty µl of ABC buffer were placed on the column before a 10 min
347 centrifugation at 14,100 x g. Ten % Trifluoroacetic acid (TFA) in ultrapure water were added

348 into the LoBind Tube to obtain 0.2 % TFA. The samples were dried in a SpeedVac up to 20 µl
349 and transferred into an injection vial.

350 *Mass spectrometry*

351 The digest was analyzed using nano-LC-ESI-MS/MS tims TOF Pro (Bruker, Billerica, MA,
352 USA) coupled with an UHPLC nanoElute (Bruker).

353 Peptides were separated by nanoUHPLC (nanoElute, Bruker) on a 75 µm ID, 25 cm C18
354 column with integrated CaptiveSpray insert (Aurora, ionopticks, Melbourne) at a flow rate of
355 400 nl/min, at 50°C. LC mobile phases A was water with 0.1% formic acid (v/v) and B ACN
356 with 0.1% formic acid (v/v). Samples were loaded directly on the analytical column at a
357 constant pressure of 800 bar. The digest (1 µl) was injected, and the organic content of the
358 mobile phase was increased linearly from 2% B to 15 % in 36 min, from 15 % B to 25% in 19
359 min, from 25% B to 37 % in 5 min and from 37% B to 95% in 5 min. Data acquisition on the
360 tims TOF Pro was performed using Hystar 5.1 and timsControl 2.0. tims TOF Pro data were
361 acquired using 100 ms TIMS accumulation time, mobility (1/K0) range from 0.6 to 1.6 Vs/cm².
362 Mass-spectrometric analysis were carried out using the parallel accumulation serial
363 fragmentation (PASEF) acquisition method. One MS spectra followed by ten PASEF MSMS
364 spectra per total cycle of 1.1 s.

365 Data analysis was performed using PEAKS Studio X Pro with ion mobility module
366 (Bioinformatics Solutions Inc., Waterloo, ON). Protein identifications were conducted using
367 PEAKS search engine with 15 ppm as parent mass error tolerance and 0.05 Da as fragment
368 mass error tolerance. Carbamidomethylation was allowed as fixed modification, oxidation of
369 methionine, histidine, tryptophan and acetylation (N-term) as variable modification. Enzyme
370 specificity was set to trypsin, and the maximum number of missed cleavages per peptide was
371 set at three. The peak lists were searched against the *E. coli*-K12 (11002 sequences) and

372 *Caulobacter* NA1000 (3863 sequences) from UNIREF 100. Peptide spectrum matches and
373 protein identifications were normalized to less than 1.0% false discovery rate.

374 The identification results were processed with the PTM profile tool from PEAKS, which
375 provides quantitative information of modified peptides compared with unmodified peptides for
376 the modification sites of the protein across all MS samples [33, 34].

377 **Circular dichroism**

378 8.95 μM of McpR was incubated with different $CuSO_4$ and Tetrakis(acetonitrile)copper(I)
379 hexafluorophosphate concentrations. Measurements were performed with a MOS-500
380 spectropolarimeter in the far-UV region (190-260 nm), using a 1 mm pathlength cell. Four scans
381 were averaged and base lines were subtracted. Secondary structure analyses were performed on
382 the circular dichroism data with the BeStSel server.

383
384

Acknowledgements

We would like to thank Jakob R. Winther for providing the rxYFP construct. We are also grateful to Valérie Charles and Carmela Aprile (CMI laboratory, NISM, UNamur) for the ICP measurements and to Virgile Neyman for technical support during the protein purification. Finally, we would like to acknowledge Jean-François Collet and Xavier De Bolle for critical reading of this manuscript and the URBM members and Johan Wouters (Chemistry Department, UNamur) for fruitful discussions. This work was supported by the University of Namur. G. L. was supported by the Belgian Fund for Industrial and Agricultural Research Associate (FRIA). Catherine Michaux and Eric Perpète thank the Belgian National Fund for Scientific Research for their respective associate and senior research associate positions.

Bibliography

1. Wadhams, G.H., and Armitage, J.P. (2004). Making sense of it all: bacterial chemotaxis. Nat Rev Mol Cell Biol *5*, 1024-1037.
2. Yang, W., and Briegel, A. (2020). Diversity of Bacterial Chemosensory Arrays. Trends Microbiol *28*, 68-80.
3. Lawaree, E., Gillet, S., Louis, G., Tilquin, F., Le Blastier, S., Cambier, P., and Matroule, J.Y. (2016). Caulobacter crescentus intrinsic dimorphism provides a prompt bimodal response to copper stress. Nat Microbiol *1*, 16098.
4. Maertens, L., Cherry, P., Tilquin, F., Van Houdt, R., and Matroule, J.Y. (2021). Environmental Conditions Modulate the Transcriptomic Response of Both Caulobacter crescentus Morphotypes to Cu Stress. Microorganisms *9*.
5. Nierman, W.C., Feldblyum, T.V., Laub, M.T., Paulsen, I.T., Nelson, K.E., Eisen, J.A., Heidelberg, J.F., Alley, M.R., Ohta, N., Maddock, J.R., et al. (2001). Complete genome sequence of Caulobacter crescentus. Proc Natl Acad Sci U S A *98*, 4136-4141.
6. Lamb, A.L., Wernimont, A.K., Pufahl, R.A., Culotta, V.C., O'Halloran, T.V., and Rosenzweig, A.C. (1999). Crystal structure of the copper chaperone for superoxide dismutase. Nat Struct Biol *6*, 724-729.
7. Drozdetskiy, A., Cole, C., Procter, J., and Barton, G.J. (2015). JPred4: a protein secondary structure prediction server. Nucleic Acids Res *43*, W389-394.
8. Berne, C., and Brun, Y.V. (2019). The Two Chemotaxis Clusters in Caulobacter crescentus Play Different Roles in Chemotaxis and Biofilm Regulation. J Bacteriol *201*.
9. Barnakov, A.N., Barnakova, L.A., and Hazelbauer, G.L. (1998). Comparison in vitro of a high- and a low-abundance chemoreceptor of Escherichia coli: similar kinase activation but different methyl-accepting activities. J Bacteriol *180*, 6713-6718.
10. Briegel, A., Wong, M.L., Hodges, H.L., Oikonomou, C.M., Piasta, K.N., Harris, M.J., Fowler, D.J., Thompson, L.K., Falke, J.J., Kiessling, L.L., et al. (2014). New insights into bacterial chemoreceptor array structure and assembly from electron cryotomography. Biochemistry *53*, 1575-1585.
11. Neumann, S., Hansen, C.H., Wingreen, N.S., and Sourjik, V. (2010). Differences in signalling by directly and indirectly binding ligands in bacterial chemotaxis. EMBO J *29*, 3484-3495.
12. Xiao, Z., Brose, J., Schimo, S., Ackland, S.M., La Fontaine, S., and Wedd, A.G. (2011). Unification of the copper(I) binding affinities of the metallo-chaperones Atx1, Atox1, and related proteins: detection probes and affinity standards. J Biol Chem *286*, 11047-11055.
13. Kahra, D., Kovermann, M., and Wittung-Stafshede, P. (2016). The C-Terminus of Human Copper Importer Ctr1 Acts as a Binding Site and Transfers Copper to Atox1. Biophys J *110*, 95-102.
14. Lee, J.W., and Helmann, J.D. (2006). The PerR transcription factor senses H2O2 by metal-catalysed histidine oxidation. Nature *440*, 363-367.
15. Tiwari, M.K., Hagglund, P.M., Moller, I.M., Davies, M.J., and Bjerrum, M.J. (2019). Copper ion / H2O2 oxidation of Cu/Zn-Superoxide dismutase: Implications for enzymatic activity and antioxidant action. Redox Biol *26*, 101262.
16. Ramteke, S.N., Walke, G.R., Joshi, B.N., Rapole, S., and Kulkarni, P.P. (2014). Effects of oxidation on redox and cytotoxic properties of copper complex of Abeta1-16 peptide. Free Radic Res *48*, 1417-1425.
17. Stadtman, E.R. (1993). Oxidation of free amino acids and amino acid residues in proteins by radiolysis and by metal-catalyzed reactions. Annu Rev Biochem *62*, 797-821.

18. Krogh, A., Larsson, B., von Heijne, G., and Sonnhammer, E.L. (2001). Predicting transmembrane protein topology with a hidden Markov model: application to complete genomes. J Mol Biol *305*, 567-580.
19. Teufel, F., Almagro Armenteros, J.J., Johansen, A.R., Gislason, M.H., Pihl, S.I., Tsirigos, K.D., Winther, O., Brunak, S., von Heijne, G., and Nielsen, H. (2022). SignalP 6.0 predicts all five types of signal peptides using protein language models. Nat Biotechnol.
20. Kelley, L.A., Mezulis, S., Yates, C.M., Wass, M.N., and Sternberg, M.J. (2015). The Phyre2 web portal for protein modeling, prediction and analysis. Nat Protoc *10*, 845-858.
21. Rubino, J.T., and Franz, K.J. (2012). Coordination chemistry of copper proteins: how nature handles a toxic cargo for essential function. J Inorg Biochem *107*, 129-143.
22. Rubino, J.T., Chenkin, M.P., Keller, M., Riggs-Gelasco, P., and Franz, K.J. (2011). A comparison of methionine, histidine and cysteine in copper(I)-binding peptides reveals differences relevant to copper uptake by organisms in diverse environments. Metallomics *3*, 61-73.
23. Chervitz, S.A., and Falke, J.J. (1996). Molecular mechanism of transmembrane signaling by the aspartate receptor: a model. Proc Natl Acad Sci U S A *93*, 2545-2550.
24. Salah Ud-Din, A.I.M., and Roujeinikova, A. (2017). Methyl-accepting chemotaxis proteins: a core sensing element in prokaryotes and archaea. Cell Mol Life Sci *74*, 3293-3303.
25. Dupont, C.L., Grass, G., and Rensing, C. (2011). Copper toxicity and the origin of bacterial resistance--new insights and applications. Metallomics *3*, 1109-1118.
26. Macomber, L., Rensing, C., and Imlay, J.A. (2007). Intracellular copper does not catalyze the formation of oxidative DNA damage in Escherichia coli. J Bacteriol *189*, 1616-1626.
27. Parkinson, J.S., Hazelbauer, G.L., and Falke, J.J. (2015). Signaling and sensory adaptation in Escherichia coli chemoreceptors: 2015 update. Trends Microbiol *23*, 257-266.
28. Khursigara, C.M., Wu, X., and Subramaniam, S. (2008). Chemoreceptors in Caulobacter crescentus: trimers of receptor dimers in a partially ordered hexagonally packed array. J Bacteriol *190*, 6805-6810.
29. Poindexter, J.S. (1981). The caulobacters: ubiquitous unusual bacteria. Microbiol Rev *45*, 123-179.
30. Evinger, M., and Agabian, N. (1977). Envelope-associated nucleoid from Caulobacter crescentus stalked and swarmer cells. J Bacteriol *132*, 294-301.
31. Ostergaard, H., Tachibana, C., and Winther, J.R. (2004). Monitoring disulfide bond formation in the eukaryotic cytosol. J Cell Biol *166*, 337-345.
32. Ducret, A., Quardokus, E.M., and Brun, Y.V. (2016). MicrobeJ, a tool for high throughput bacterial cell detection and quantitative analysis. Nat Microbiol *1*, 16077.
33. Meier, F., Brunner, A.D., Koch, S., Koch, H., Lubeck, M., Krause, M., Goedecke, N., Decker, J., Kosinski, T., Park, M.A., et al. (2018). Online Parallel Accumulation-Serial Fragmentation (PASEF) with a Novel Trapped Ion Mobility Mass Spectrometer. Mol Cell Proteomics *17*, 2534-2545.
34. Zhang, J., Xin, L., Shan, B., Chen, W., Xie, M., Yuen, D., Zhang, W., Zhang, Z., Lajoie, G.A., and Ma, B. (2012). PEAKS DB: de novo sequencing assisted database search for sensitive and accurate peptide identification. Mol Cell Proteomics *11*, M111 010587.

Supporting information

Caulobacter crescentus genome is predicted to encode two chemotaxis clusters including genes coding for CheA histidines kinases, CheY response regulators, CheW adaptors, CheB methylesterases, CheR methytransferases, McpA and McpK and other uncharacterized Che proteins. Most of the studies conducted in *C. crescentus* so far focused on the major chemotaxis cluster (cluster 1) (1-4) while the second alternate chemotaxis cluster (cluster 2) was only recently investigated (1). These studies concluded that the cluster 1 is essential for chemotaxis, while cluster 1 and cluster 2 are involved in biofilm formation and holdfast production (1, 2). Consistent with these observations, CheAI (cluster 1 CheA) turns out to be the main histidine kinase involved in chemotaxis while the exact function of CheAII (cluster 2 CheA) remains unknown[1]. In order to determine which CheA is involved in Cu-chemotaxis, we constructed the Δ*cheAI*, Δ*cheAII* and Δ*cheAI-II* mutants and assessed their chemotactic behavior to Cu by LCI (**Fig. 1**). The Δ*cheAI* mutant completely lost its chemotactic response to Cu, while the Δ*cheAII* mutant displayed a WT phenotype. Accordingly, the Δ*cheAI-II* double mutant showed a similar behavior to the Δ*cheAI* mutant. These data confirm that the CheAI histidine kinase is the main histidine kinase involved in Cu chemotaxis.

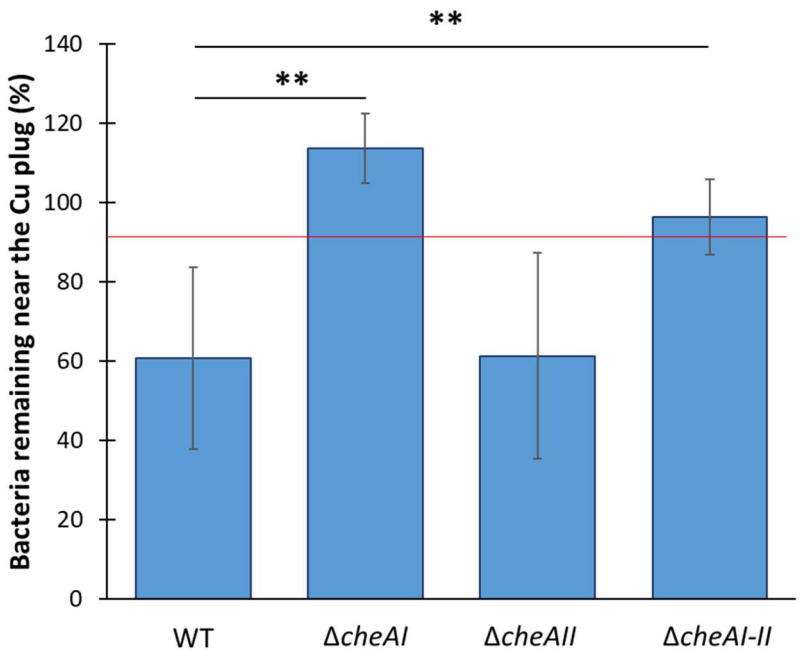

Figure 1: CheAI is the main histidine kinase involved in Cu chemotaxis. Percentage of WT, Δ*cheAI*, Δ*cheAII* and Δ*cheAI-II* SW cells remaining in the vicinity of the Cu plug after 25 min. An arbitrary threshold of 10% flight (corresponding to 90% of cells remaining in the vicinity of the Cu plug) is indicated in red. Mean +/- s.d., at least 3 biological replicates. *p-values* were calculated using an ANOVA (* $p < 0.05$, ** $p < 0.01$, *** $p < 0.001$).

References

1 Alley, M. R., Maddock, J. R. & Shapiro, L. Polar localization of a bacterial chemoreceptor. *Genes Dev* **6**, 825-836, doi:10.1101/gad.6.5.825 (1992).

2 Alley, M. R., Maddock, J. R. & Shapiro, L. Requirement of the carboxyl terminus of a bacterial chemoreceptor for its targeted proteolysis. *Science* **259**, 1754-1757, doi:10.1126/science.8456303 (1993).

3 Tsai, J. W. & Alley, M. R. Proteolysis of the McpA chemoreceptor does not require the *Caulobacter* major chemotaxis operon. *J Bacteriol* **182**, 504-507, doi:10.1128/JB.182.2.504-507.2000 (2000).

4 Tsai, J. W. & Alley, M. R. Proteolysis of the *Caulobacter* McpA chemoreceptor is cell cycle regulated by a ClpX-dependent pathway. *J Bacteriol* **183**, 5001-5007, doi:10.1128/JB.183.17.5001-5007.2001 (2001).

5 Berne, C. & Brun, Y. V. The Two Chemotaxis Clusters in *Caulobacter crescentus* Play Different Roles in Chemotaxis and Biofilm Regulation. *J Bacteriol* **201**, doi:10.1128/JB.00071-19 (2019).

Figure 1

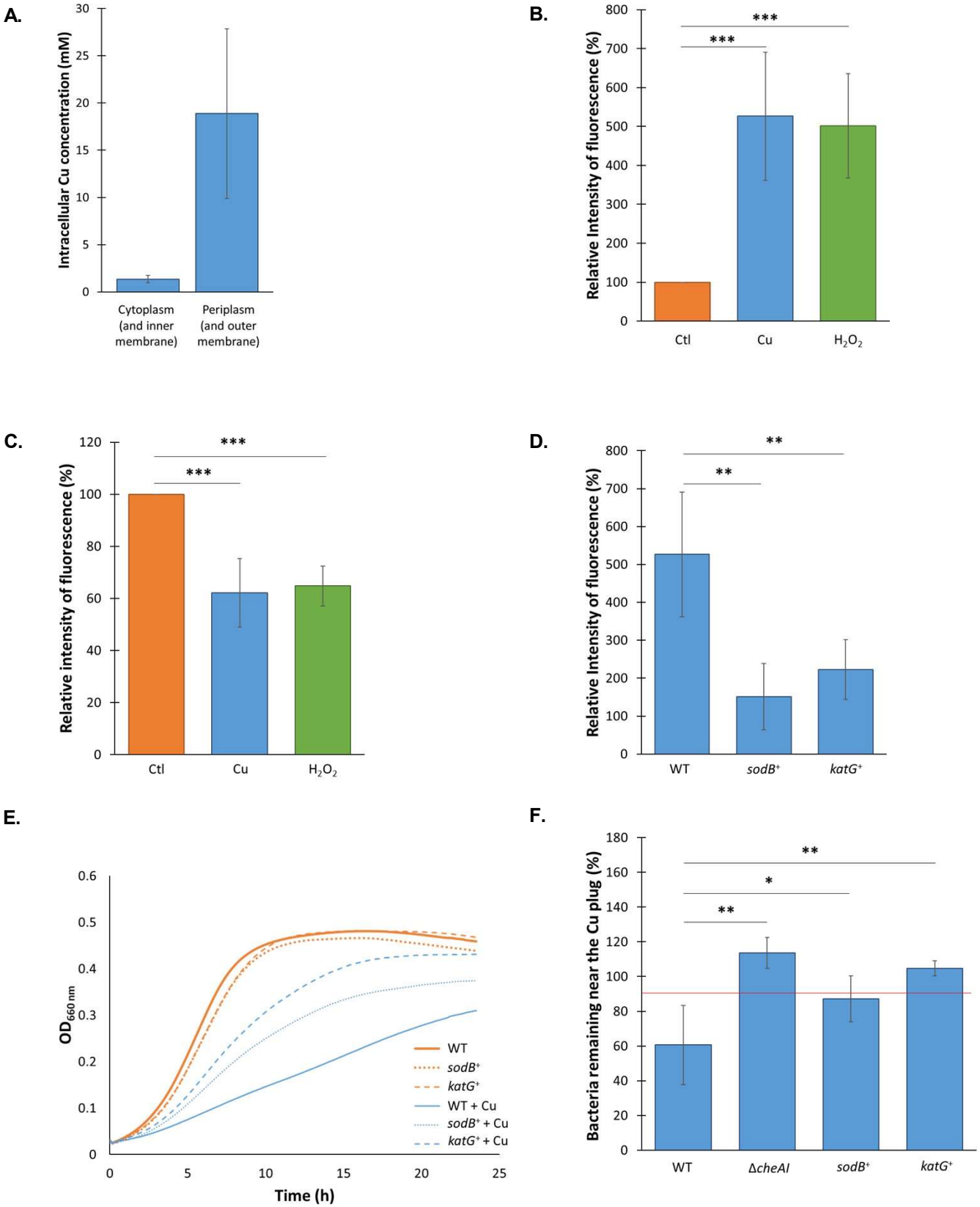
A.
Intracellular Cu concentration (mM)
30
25
20
15
10
5
0
Cytoplasm (and inner membrane)
Periplasm (and outer membrane)
B.
Relative Intensity of fluorescence (%)
800
700
600
500
400
300
200
100
0
***
***
Ctl
Cu
H2O2
C.
Relative intensity of fluorescence (%)
120
100
80
60
40
20
0
***
***
Ctl
Cu
H2O2
D.
Relative Intensity of fluorescence (%)
800
700
600
500
400
300
200
100
0
**
**
WT
sodB+
katG+
E.
OD660 nm
0.6
0.5
0.4
0.3
0.2
0.1
0
0
5
10
15
20
25
Time (h)
WT
sodB+
katG+
WT + Cu
sodB+ + Cu
katG+ + Cu
F.
Bacteria remaining near the Cu plug (%)
180
160
140
120
100
80
60
40
20
0
**
*
**
WT
ΔcheAI
sodB+
katG+

Figure 1: Cu-induced ROS sustain Cu chemotaxis. A. Intracellular Cu concentration in the cytoplasm (and inner membrane fraction) and in the periplasm (and outer membrane fraction) in SW cells exposed to 175 µM Cu for 5 min. **B.** Relative fluorescence intensity of SW cells incubated with 5 µM CellROX Deep Red probe and exposed to 175 µM Cu or 400 µM H_2O_2. **C.** Relative fluorescence intensity of SW cells expressing the rxYFP biosensor and exposed to 175 µM Cu or 400 µM H_2O_2 for 20 min. **D.** Relative fluorescence intensity of WT SW cells and SW cells overexpressing SodB (*sodB*$^+$) and KatG (*katG*$^+$) incubated with 5 µM CellROX Deep Red probe and exposed to 175 µM Cu. **E.** Growth profiles at $OD_{660\ nm}$ of WT, *sodB*$^+$ and *katG*$^+$ strains in PYE (orange) and exposed to 175 µM Cu (blue). **F.** Percentage of WT, Δ*cheAI*, *sodB*$^+$ and *katG*$^+$ SW cells in the vicinity of the Cu plug after 25 min. An arbitrary threshold of 10% flight (corresponding to 90% of cells remaining in the vicinity of the Cu plug) is indicated in red. Mean +/- s.d., at least 3 biological replicates. *p- values* were calculated using an ANOVA when appropriate (* $p < 0.05$, ** $p < 0.01$, *** $p < 0.001$).

Figure 2

A.

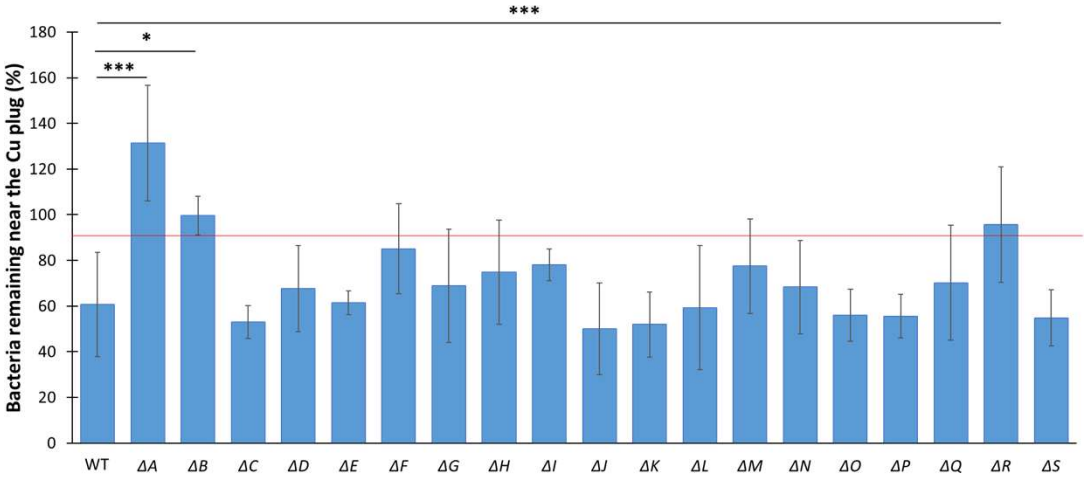
***
*
***
Bacteria remaining near the Cu plug (%)
180
160
140
120
100
80
60
40
20
0
WT
ΔA
ΔB
ΔC
ΔD
ΔE
ΔF
ΔG
ΔH
ΔI
ΔJ
ΔK
ΔL
ΔM
ΔN
ΔO
ΔP
ΔQ
ΔR
ΔS

B.

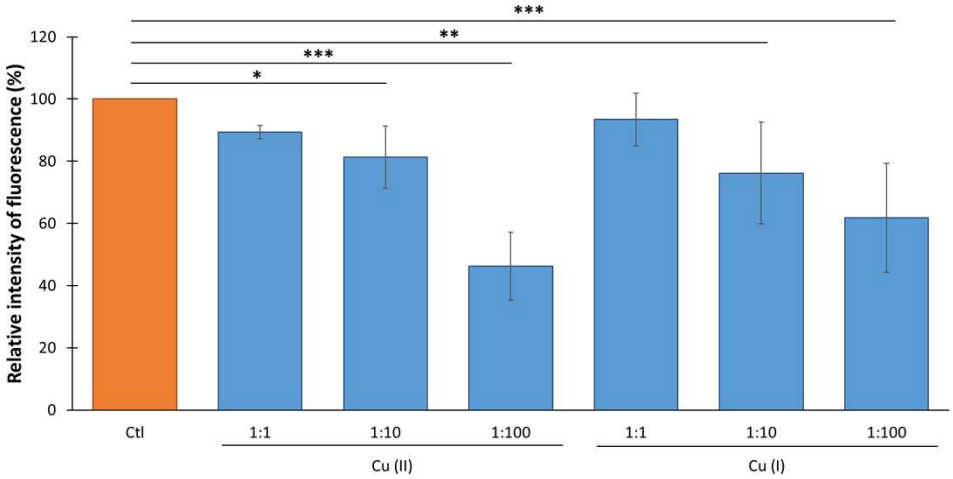
***
**
***
*
Relative intensity of fluorescence (%)
120
100
80
60
40
20
0
Ctl
1:1
1:10
1:100
1:1
1:10
1:100
Cu (II)
Cu (I)

C.

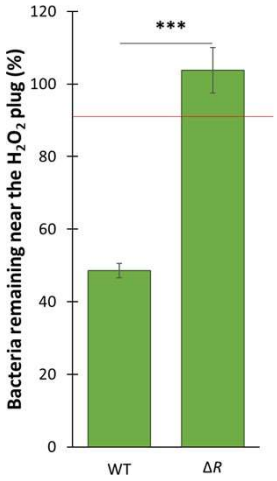
***
Bacteria remaining near the H_2O_2 plug (%)
120
100
80
60
40
20
0
WT
ΔR

Figure 2: McpR is involved in Cu chemotaxis and Cu binding. A. Percentage of WT and Δ*mcp (mcpA* to *mcpS)* SW cells remaining in the vicinity of the Cu plug after 25 min. An arbitrary threshold of 10% flight (corresponding to 90% of cells remaining in the vicinity of the Cu plug) is indicated in red. **B.** Relative intrinsic fluorescence intensity of purified McpR (3.58 μM) incubated with Cu(II) and Cu(I) at 1:1, 1:10 and 1:100 ratios. **C.** Percentage of WT and Δ*mcpR* SW cells remaining in the vicinity of the H_2O_2 plug after 25 min. An arbitrary threshold of 10% flight (corresponding to 90% of cells remaining in the vicinity of the H_2O_2 plug) is indicated in red. Mean +/- s.d., at least 3 biological replicates. *p-values* were calculated using an ANOVA when appropriate (* $p < 0.05$, ** $p < 0.01$, *** $p < 0.001$).

Figure 3

A.

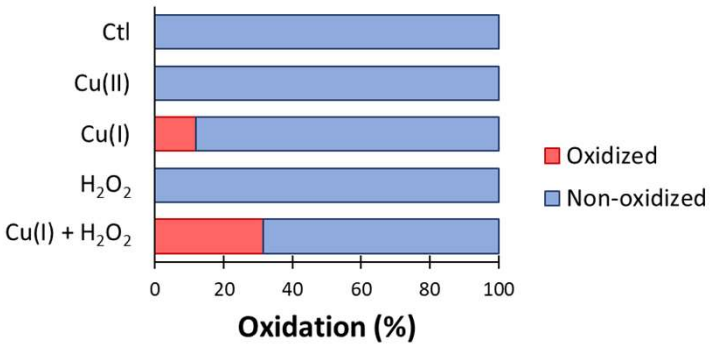

B.

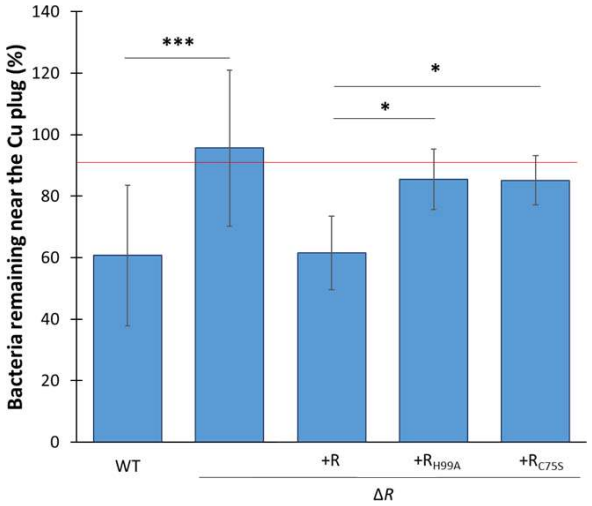

C.

	Cu(I)	Cu(II)
	*K*d (µM)	*K*d (µM)
McpR	48 ± 10	37 ± 9
$McpR_{H99A}$	451 ± 205	213 ± 140
$McpR_{C75S}$	168 ± 83	46 ± 23

D.

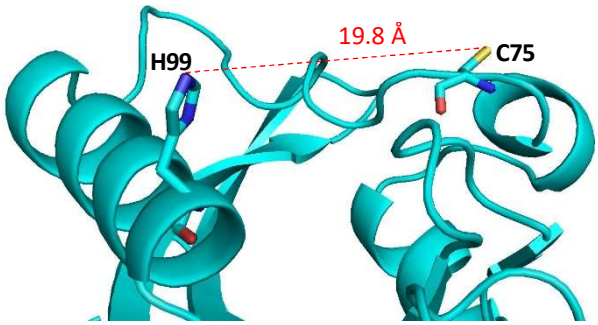

E.

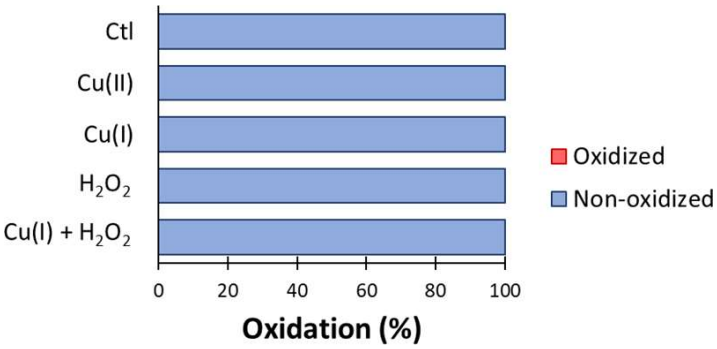

F.

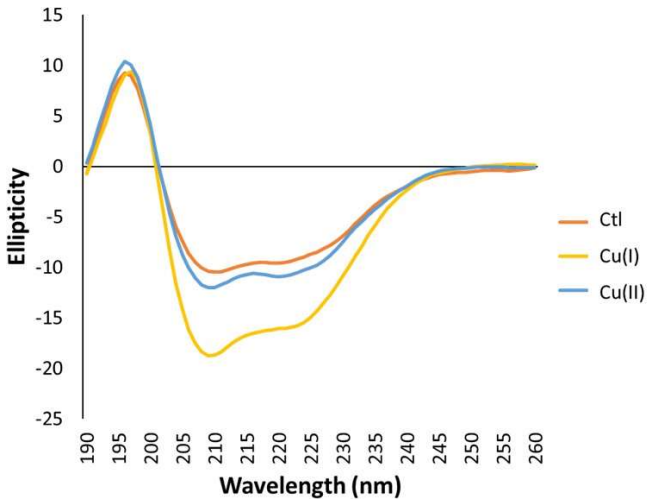

Figure 3: Cu cycling modulates its coordination by the H99 and C75 residues. A. Percentage of oxidation of the H99 residue from purified McpR incubated with Cu(II), Cu(I), H_2O_2 and Cu(I)+H_2O_2 at a 1:100 ratio. **B.** Percentage of SW cells with a WT, Δ*mcpR* and Δ*mcpR* overexpressing McpR, $McpR_{H99A}$ or $McpR_{C75S}$ background remaining in the vicinity of the Cu plug after 25 min. An arbitrary threshold of 10% flight (corresponding to 90% of cells remaining in the vicinity of the Cu plug) is indicated in red. Mean +/- s.d., at least 3 biological replicates. *p-values* were calculated using an ANOVA (* $p < 0.05$, ** $p < 0.01$, *** $p < 0.001$). **C.** Measure, by intrinsic fluorescence, of the *K*d values of purified McpR, $McpR_{H99A}$ and $McpR_{C75S}$ (1.79 µM) incubated with 0 to 500 µM Cu(I) and Cu(II). Mean +/- s.d. **D.** 3D structure prediction of the sensor domain of McpR by Phyre 2. H99 and C75 residues are highlighted. The distance was measured with PyMOL viewer **E.** Percentage of oxidation of the H99 residue from purified $McpR_{C75S}$ incubated Cu(II), Cu(I), H_2O_2 and Cu(I)+H_2O_2 at a 1:100 ratio. **F.** Circular Dichroism spectra of purified McpR (8.95 µM) incubated with Cu(I) and Cu(II) at a 1:100 ratio.

Figure 4

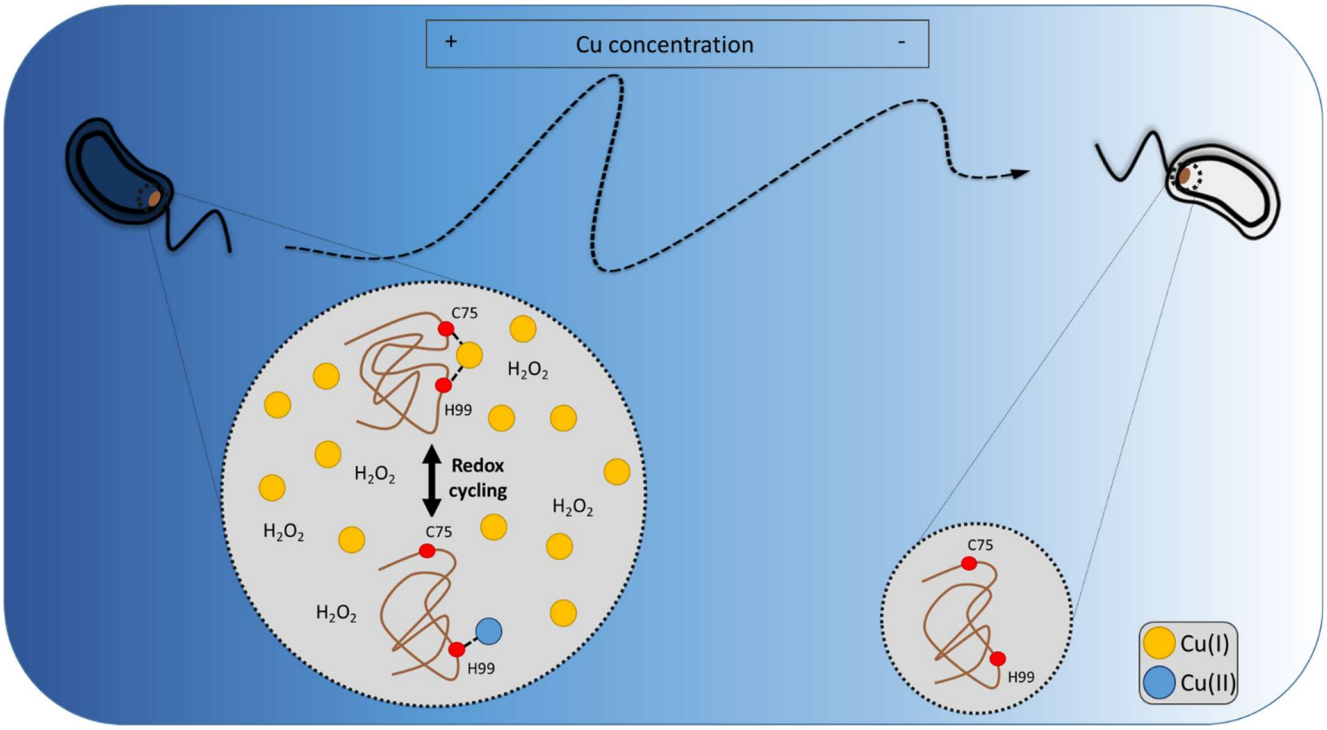

Figure 4: Hypothetical model of Cu sensing by McpR. SW cell exposure to Cu increases the cytoplasmic Cu concentration, leading to the generation of H_2O_2 (left). In addition, high cytoplasmic Cu content favors Cu(I) coordination by the C75 and H99 residues within the cytoplasmic McpR, triggering a conformational change of the chemoreceptor. Cu(II) binding to H99 residue has no impact on McpR apo-like conformation, suggesting that a redox-cycling of the McpR-bound Cu atom could modulate McpR conformation and very likely its activity. This redox Cu cycling would be maintained along the extracellular Cu gradient until the SW cell reaches a Cu-poor environment (right). Under these conditions, the cytoplasmic Cu concentration together with the ROS level would return to their basal level and the labile Cu binding to McpR would be hindered, bringing McpR to its apo form conformation.

Figure S1

A.

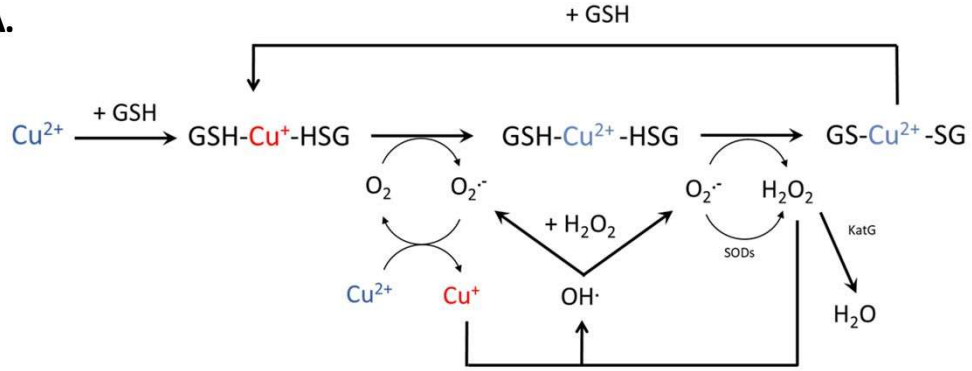
+ GSH
Cu2+
+ GSH
GSH-Cu+-HSG
GSH-Cu2+-HSG
GS-Cu2+-SG
O2
O2·-
O2·-
H2O2
+ H2O2
KatG
SODs
Cu2+
Cu+
OH·
H2O

B.

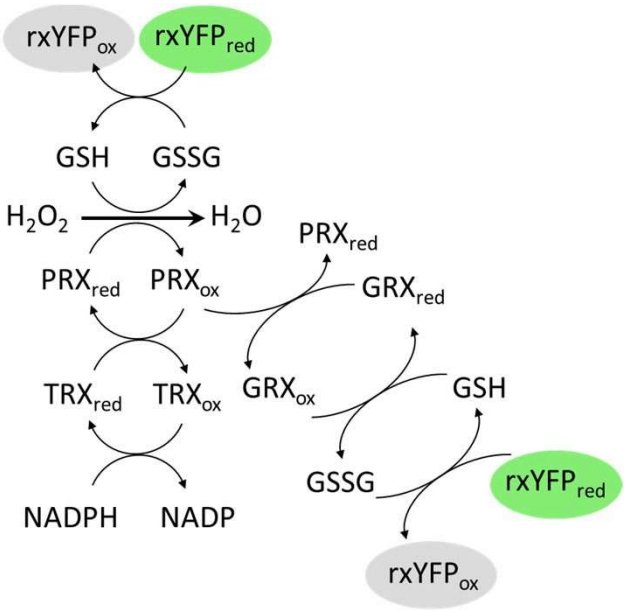
rxYFPox
rxYFPred
GSH
GSSG
H2O2
H2O
PRXred
PRXred
PRXox
GRXred
TRXred
TRXox
GRXox
GSH
GSSG
rxYFPred
NADPH
NADP
rxYFPox

Figure S1: Potential pathways leading to ROS production by Cu. A. *In vitro* generation of Cu-induced ROS by Fenton-like reaction and Haber-Weiss cycles. The Cu-GSH complexes may also trigger ROS production (27, 28). The SODs and KatG are involved in $O_2^{\bullet -}$ and H_2O_2 detoxification, respectively **B.** The rxYFP biosensor is in equilibrium with the GSH pool. GSH is involved in different ways in ROS buffering. As a result, ROS production triggers an increase of the GS-SG pool, which will be partially reduced to GSH by using rxYFP as an electron donor. The resulting oxidized rxYFP will lose its fluorescence properties. GSH (glutathione), PRX (Peroxiredoxins), TRX (thioredoxin) and GRX (glutaredoxin).

Figure S2

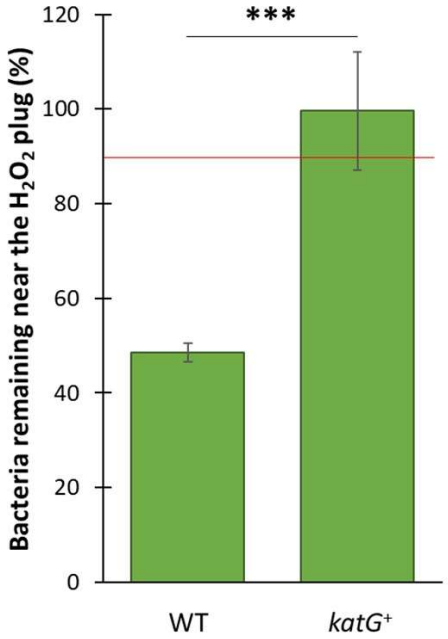
***
120
100
80
60
40
20
0
Bacteria remaining near the H_2O_2 plug (%)
WT
katG⁺

Figure S2: Overexpression of KatG prevents H_2O_2 chemotaxis. Percentage of WT and *katG*$^+$ SW cells remaining in the vicinity of the H_2O_2 plug after 25 min. An arbitrary threshold of 10% flight (corresponding to 90% of cells remaining in the vicinity of the H_2O_2 plug) is indicated in red. Mean +/- s.d., at least 3 biological replicates. *p-values* were calculated using an ANOVA (* $p < 0.05$, ** $p < 0.01$, *** $p < 0.001$).

Figure S3

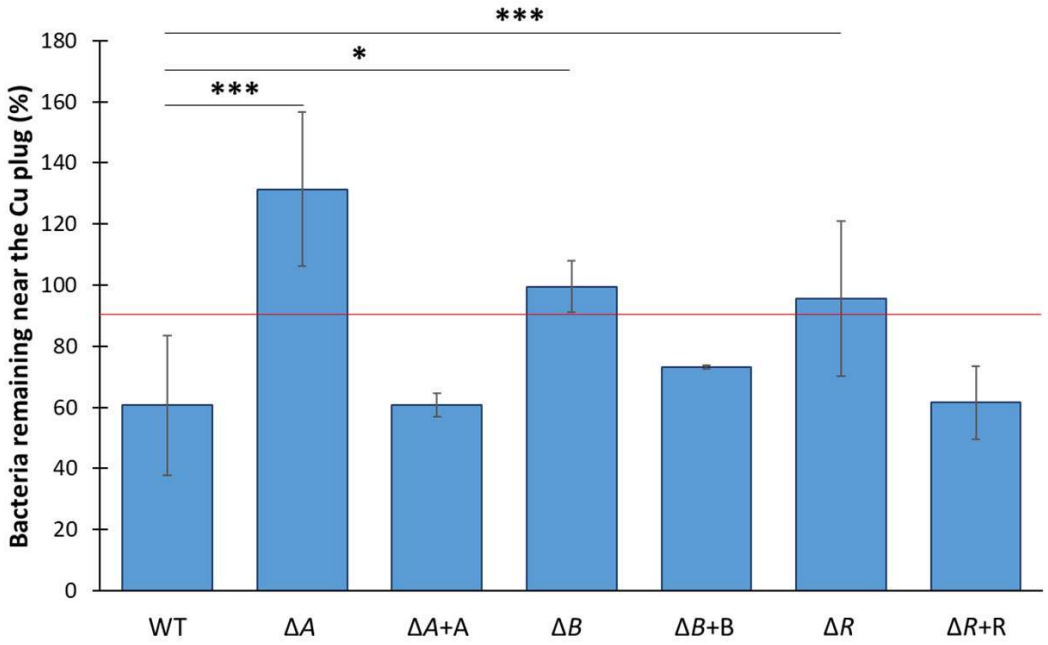
***
*
***
Bacteria remaining near the Cu plug (%)
180
160
140
120
100
80
60
40
20
0
WT
ΔA
ΔA+A
ΔB
ΔB+B
ΔR
ΔR+R

Figure S3: McpA, McpB and McpR are potentially involved in Cu chemotaxis. Percentage of WT, Δ*mcpA*, Δ*mcpA* overexpressing McpA, Δ*mcpB*, Δ*mcpB* overexpressing McpB, Δ*mcpR* and Δ*mcpR* overexpressing McpR SW cells remaining in the vicinity of the Cu plug after 25 min. An arbitrary threshold of 10% flight (corresponding to 90% of cells remaining in the vicinity of the Cu plug) is indicated in red. Mean +/- s.d., at least 3 biological replicates. *p-values* were calculated using an ANOVA (* $p < 0.05$, ** $p < 0.01$, *** $p < 0.001$).

Figure S4

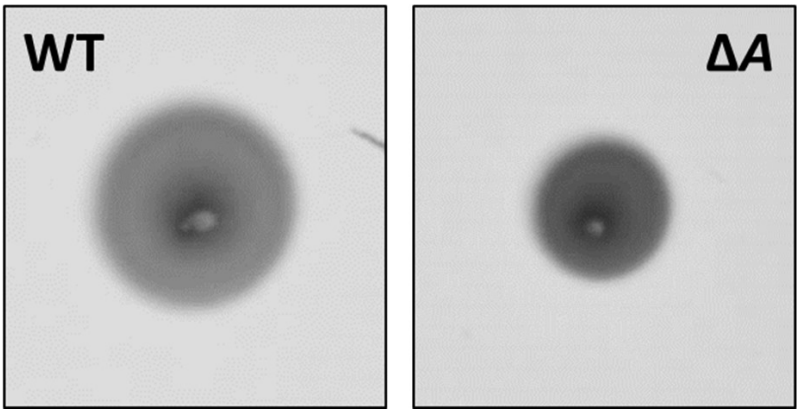

Figure S4: The Δ*mcpA* mutant is defective in chemotaxis. Chemotaxis-driven swarming pattern of the WT and Δ*mcpA* strains.

Figure S5

A.

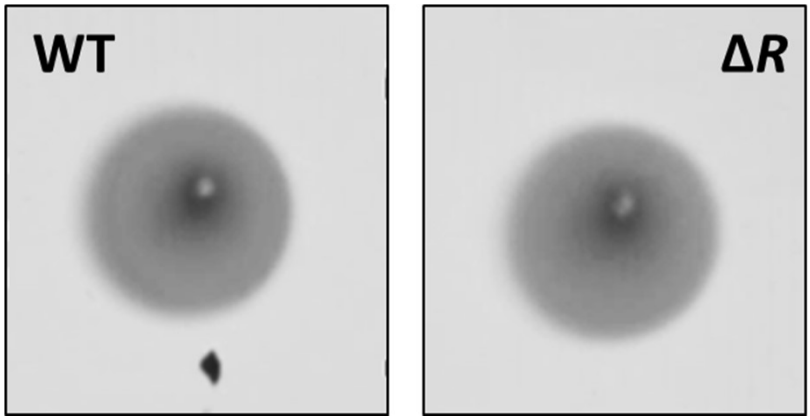
WT
ΔR

B.

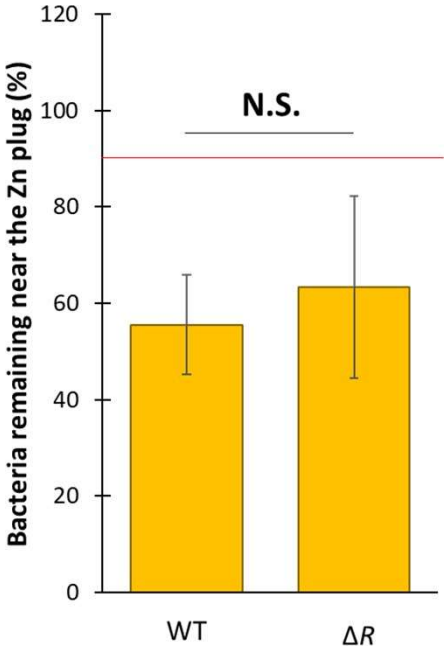
Bacteria remaining near the Zn plug (%)
120
100
80
60
40
20
0
N.S.
WT
ΔR

Figure S5: The chemotactic machinery is functional in the Δ*mcpR* mutant. A. Chemotaxis-driven swarming pattern of the WT and Δ*mcpR* strains. **B.** Percentage of WT and Δ*mcpR* SW cells remaining in the vicinity of the Zn plug after 25 min. An arbitrary threshold of 10% flight (corresponding to 90% of cells remaining in the vicinity of the Zn plug) is indicated in red. Mean +/- s.d., at least 3 biological replicates. *p-values* were calculated using a *t-test* (* $p < 0.05$, ** $p < 0.01$, *** $p < 0.001$).

Figure S6

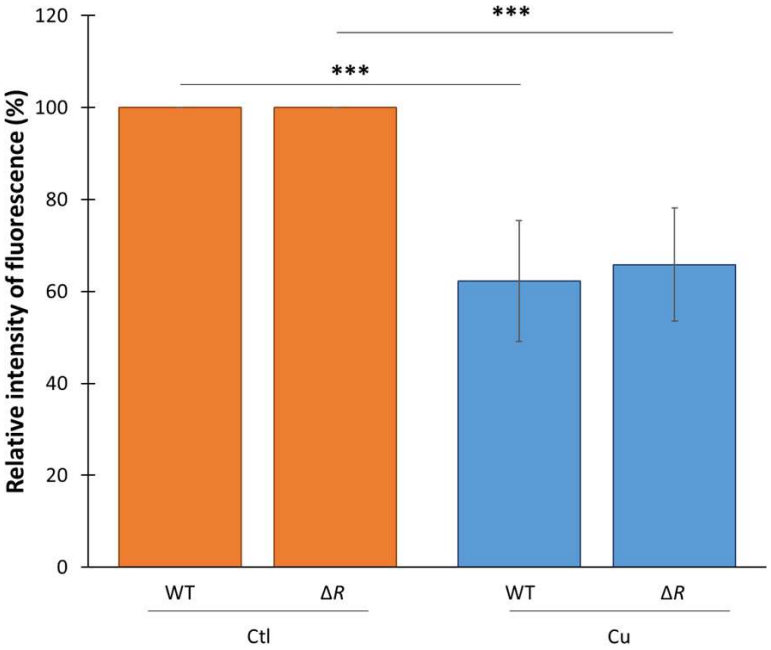
120
100
80
60
40
20
0
Relative intensity of fluorescence (%)
***
***
WT
ΔR
WT
ΔR
Ctl
Cu

Figure S6: The Cu-induced oxidative stress is not affected in the Δ*mcpR* mutant. Relative intensity of fluorescence of the WT and Δ*mcpR* SW cells overexpressing the rxYFP biosensor and exposed to 175 µM Cu for 20 min. Mean +/- s.d., at least 3 biological replicates. *p- values* were calculated using a *t-test* (* $p < 0.05$, ** $p < 0.01$, *** $p < 0.001$).

Figure S7

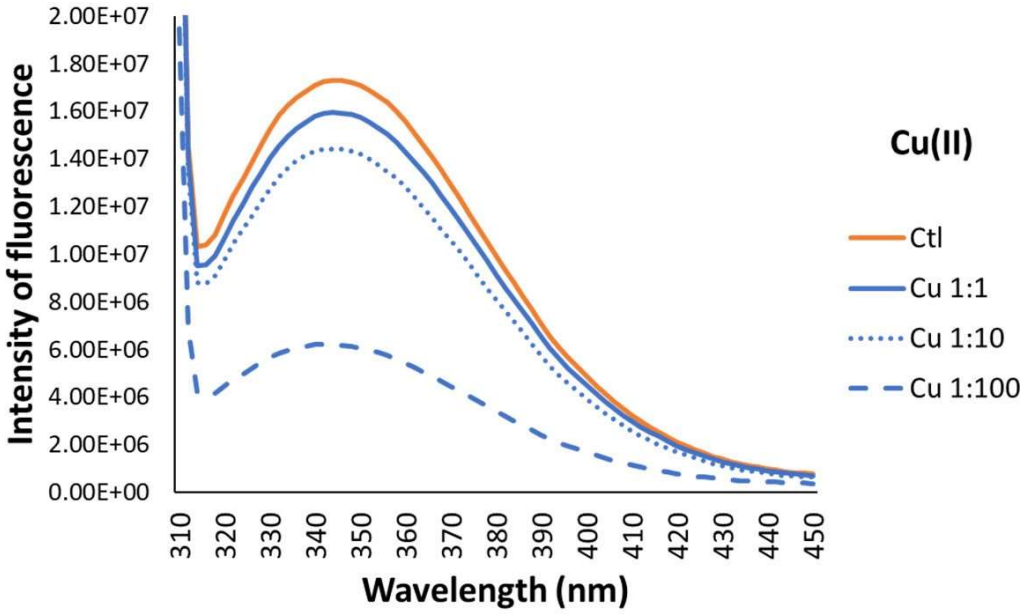
Intensity of fluorescence
2.00E+07
1.80E+07
1.60E+07
1.40E+07
1.20E+07
1.00E+07
8.00E+06
6.00E+06
4.00E+06
2.00E+06
0.00E+00
310
320
330
340
350
360
370
380
390
400
410
420
430
440
450
Wavelength (nm)
Cu(II)
Ctl
Cu 1:1
Cu 1:10
Cu 1:100

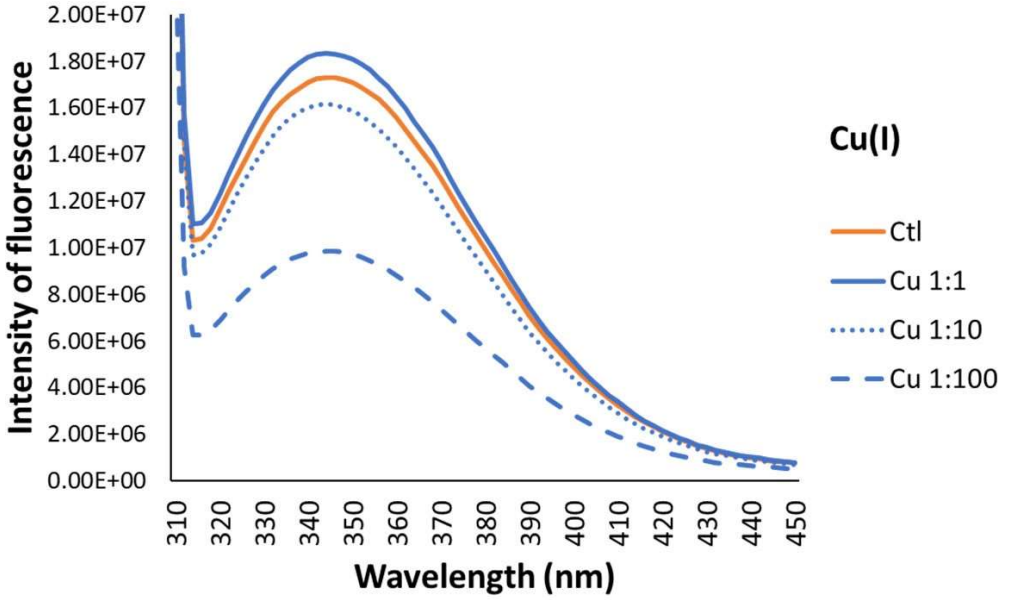
Intensity of fluorescence
2.00E+07
1.80E+07
1.60E+07
1.40E+07
1.20E+07
1.00E+07
8.00E+06
6.00E+06
4.00E+06
2.00E+06
0.00E+00
310
320
330
340
350
360
370
380
390
400
410
420
430
440
450
Wavelength (nm)
Cu(I)
Ctl
Cu 1:1
Cu 1:10
Cu 1:100

Figure S7: Representative fluorescence spectra of purified McpR. Representative intrinsic fluorescence spectra upon 280 nm excitation of purified McpR (3.58 μM) incubated with Cu(II) (top) and Cu(I) (bottom) at 1:1, 1:10 and 1:100 ratios.

Figure S8

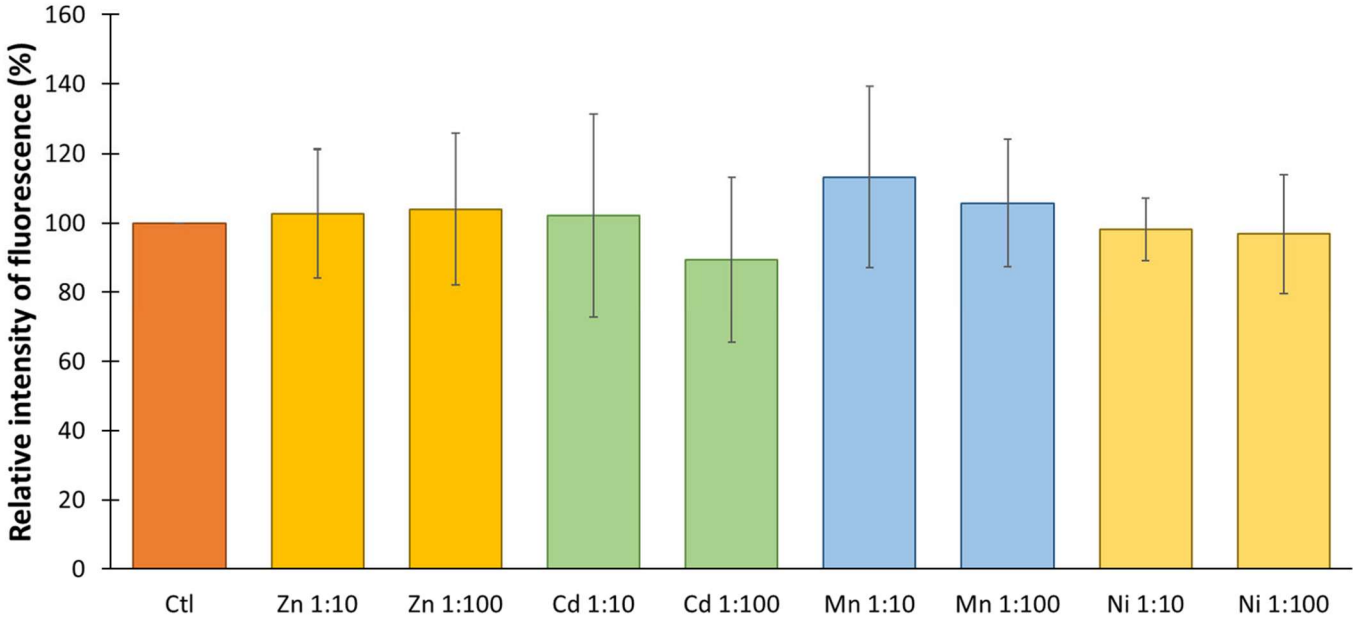
Relative intensity of fluorescence (%)
160
140
120
100
80
60
40
20
0
Ctl
Zn 1:10
Zn 1:100
Cd 1:10
Cd 1:100
Mn 1:10
Mn 1:100
Ni 1:10
Ni 1:100

Figure S8: Zn, Cd, Mn and Ni do not directly bind to McpR. Relative intrinsic fluorescence of purified McpR (3.58 μM) incubated with $ZnSO_4$, $CdSO_4$, $MnSO_4$ and $NiSO_4$ at 1:10 and 1:100 ratios. Mean +/- s.d., at least 3 biological replicates. *p-values* were calculated using an ANOVA and were not significant ($p > 0.05$).

Figure S9

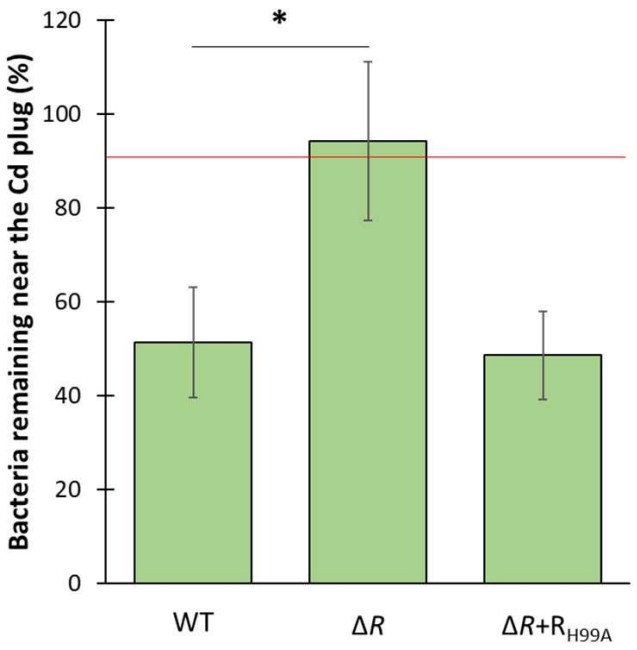
*
120
100
80
60
40
20
0
Bacteria remaining near the Cd plug (%)
WT
ΔR
ΔR+R$_{H99A}$

Figure S9: The McpR$_{H99A}$ mutant is still proficient for Cd chemotaxis. Percentage of WT, Δ*mcpR* and Δ*mcpR* overexpressing McpR$_{H99A}$ SW cells remaining in the vicinity of the Cd plug after 25 min. An arbitrary threshold of 10% flight (corresponding to 90% of cells remaining in the vicinity of the Cd plug) is indicated in red. Mean +/- s.d., at least 3 biological replicates. *p-values* were calculated using an ANOVA (* $p < 0.05$, ** $p < 0.01$, *** $p < 0.001$).

Figure S10

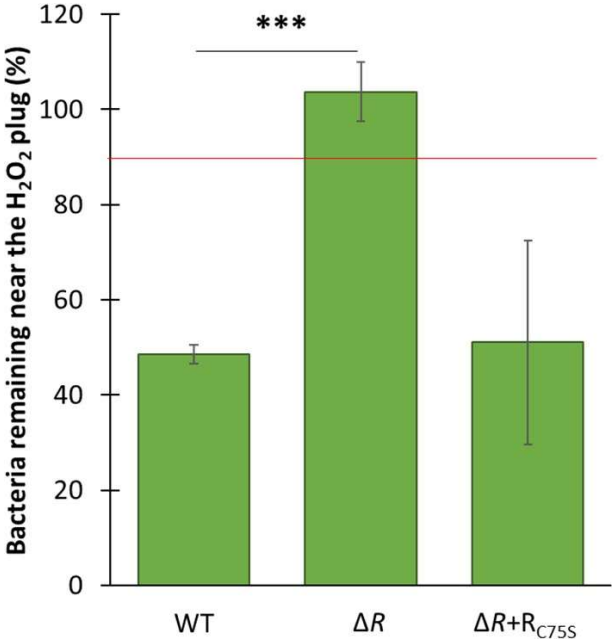
***
120
100
80
60
40
20
0
Bacteria remaining near the H_2O_2 plug (%)
WT
Δ*R*
Δ*R*+R_{C75S}

Figure S10: The $McpR_{C75S}$ mutant is still proficient for H_2O_2 chemotaxis. Percentage of WT, Δ*mcpR* and Δ*mcpR* overexpressing $McpR_{C75S}$ SW cells remaining in the vicinity of the H_2O_2 plug after 25 min. An arbitrary threshold of 10% flight (corresponding to 90% of cells remaining in the vicinity of the H_2O_2 plug) is indicated in red. Mean +/- s.d., at least 3 biological replicates, except for Δ*mcpR* overexpressing $McpR_{C75S}$ (2 biological replicates). *p-values* were calculated using an ANOVA (* $p < 0.05$, ** $p < 0.01$, *** $p < 0.001$).

Table S1

Strains	**Relevant genotype or description**	**References**
C. crescentus		
WT	CB15N (or NA1000), synchronizable variant strain of CB15	(Evinger and Agabian, 1977)
WTrxYFP	WT strain carrying the *rxYFP* gene on the pJS14 under the control of the lac promoter; CmR	This study
ΔcheAI	Knockout strain for *cheAI* gene (CCNA_XXX)	This study
ΔA	Knockout strain for *mcpA* gene	This study
ΔA+A	Knockout strain for *mcpA* gene carrying a copy of *mcpA* on the pMR10 under the control of the lac promoter; KanR	This study
ΔB	Knockout strain for *mcpB* gene	This study
ΔB+B	Knockout strain for *mcpB* gene carrying a copy of *mcpB* on the pMR10 under the control of the lac promoter; KanR	This study
ΔC	Knockout strain for *mcpC* gene	This study
ΔD	Knockout strain for *mcpD* gene	This study
ΔE	Knockout strain for *mcpE* gene	This study
ΔF	Knockout strain for *mcpF* gene	This study
ΔG	Knockout strain for *mcpG* gene	This study
ΔH	Knockout strain for *mcpH* gene	This study
ΔI	Knockout strain for *mcpI* gene	This study
ΔJ	Knockout strain for *mcpJ* gene	This study
ΔK	Knockout strain for *mcpK* gene	This study
ΔL	Knockout strain for *mcpL* gene	This study
ΔM	Knockout strain for *mcpM* gene	This study
ΔN	Knockout strain for *mcpN* gene	This study
ΔO	Knockout strain for *mcpO* gene	This study
ΔP	Knockout strain for *mcpP* gene	This study
ΔQ	Knockout strain for *mcpQ* gene	This study
ΔR	Knockout strain for *mcpR* gene	This study
ΔRrxYFP	Knockout strain for *mcpR* gene carrying the *rxYFP* gene on the pJS14 under the control of the lac promoter; CmR	This study
ΔR+R	Knockout strain for *mcpR* gene carrying a copy of *mcpR* on the pMR10 under the control of the lac promoter; KanR	This study
ΔR+RH99A	Knockout strain for *mcpR* gene carrying a copy of *mcpR* with the mutation H99A on the pMR10 under the control of the lac promoter; KanR	This study
ΔR+RC75S	Knockout strain for *mcpR* gene carrying a copy of *mcpR* with the mutation C75S on the pMR10 under the control of the lac promoter; KanR	This study
ΔS	Knockout strain for *mcpS* gene	This study
sodB+	WT strain carrying a copy of *sodB* on the pMR10 under the control of the lac promoter; KanR	This study
katG+	WT strain carrying a copy of *katG* on the pMR10 under the control of the lac promoter; KanR	This study
WTrxYFP	WT strain carrying the *rxYFP* gene on the pJS14 under the control of the lac promoter; CmR	This study
E. coli		
S17-1	RP4-2, Tc::Mu, KM-Tn7, for plasmid mobilization	
BL21	BL21 *E. coli* strain used for overexpression of proteins	
Plasmids	**Relevant genotype or description**	
pNPTS138	mobRP4+ ori-R6K sacB; integrative vector in *C. crescentus* for in-frame deletions; KanR	
pMR10	DH10B strain carrying the pMR10 low copy number replicative cloning vector in *E. coli* and *C. crescentus* ; KanR	
pJS14	DH10B strain carrying the pJS14 medium copy number replicative cloning vector in *E. coli* and *C. crescentus* ; CmR	
pET28a	BL21 strain carrying the pET28a high copy number replicative cloning vector in *E. coli* ; KanR	

Table S1: Strains and plasmids